Magnetic Resonance Imaging 57 (2019) 259–270

Contents lists available at ScienceDirect

Magnetic Resonance Imaging

journal homepage: www.elsevier.com/locate/mri

Original contribution

Dependence of the frequency distribution around a vessel on the voxel orientation

L.R. Buschle[a,b,c], T. Kampf[d,e], F.T. Kurz[a,b], P. Vogel[d,f], F. Piekarek[d], V.J.F. Sturm[b], M. Pham[e], H.-P. Schlemmer[a], C.H. Ziener[a,b,*]

[a] German Cancer Research Center, E010 Radiology, INF 280, Heidelberg D-69120, Germany
[b] Heidelberg University Hospital, Dept. of Neuroradiology, INF 400, Heidelberg D-69120, Germany
[c] Heidelberg University, Faculty of Physics and Astronomy, INF 227, D-69120 Heidelberg, Germany
[d] University of Würzburg, Dept. of Experimental Physics 5, Am Hubland, D-97074 Würzburg, Germany
[e] Würzburg University Hospital, Dept. of Neuroradiology, Josef-Schneider-Straße 11, Würzburg D-97080, Germany
[f] Würzburg University Hospital, Dept. of Diagnostic and Interventional Radiology, Oberdürrbacher Straße 6, Würzburg D-97080, Germany

ARTICLE INFO

Keywords:
Susceptibility effects
Dipole field
Frequency distribution
Blood oxygenation

ABSTRACT

In this work the frequency distribution around a vessel inside a cubic voxel is investigated. Therefore, the frequency distribution is calculated in dependence on the orientation of the voxel according to the external magnetic field. The frequency distribution exhibits an interesting peak structure that cannot be explained by the established Krogh's vessel model. The results were validated with phantom measurements and in vivo measurements that agree very well with the developed theory.

1. Introduction

In MRI, biological tissue is usually characterized by relaxation times. Especially the gradient echo relaxation time T_2^* is closely connected with the offresonance frequency distribution of a magnetic inhomogeneity inside a voxel and, thus, contains information of the tissue structure [1]. The gradient echo relaxation time T_2^* consists of two components: an irreversible spin-spin interaction and a part associated with the static field inhomogeneities. The latter part is the subject of this work. To understand its contribution, one should recall the Larmor relation $\omega(\mathbf{r}) = \gamma B(\mathbf{r})$, where $B(\mathbf{r})$ is the local magnetic field, γ is the gyromagnetic ratio and $\omega(\mathbf{r})$ is the local resonance frequency of the nuclear spins. If the magnetic field is spatial dependent, the local Larmor frequency is as well. Such position dependent fields are called field inhomogeneities and can be caused by boundaries between tissues of different susceptibility. Often the structures which cause these field inhomogeneities are below the resolution of modern MR scanners and, thus, direct observation of the structure itself is not possible. Only the signal averaged over the voxel can be measured in a MR experiment. For this reason, a detailed understanding of the signal formation inside a voxel is imperative to obtain information about the structure of the tissue. A prominent example for such a case is the BOLD effect where the susceptibility difference between deoxygenated blood and surrounding tissue generates a local magnetic field $B(\mathbf{r})$ [2-4] which leads to enhanced dephasing around the vessel. This enhanced dephasing results in a shorter T_2' relaxation time which therefore contains information about the blood oxygenation [5]. However, the characterization of the signal time evolution by simple exponentials using relaxation times is sometimes only a crude approximation of the experimentally measured signal behaviour. Especially for short echo times this exponential approximation does not describe the signal behaviour sufficiently since a Gaussian signal decay $S(t)/S(0) \approx 1 - \gamma^2\langle B^2(\mathbf{r})\rangle t^2/2$ holds in this case [6,7]. A better description of the real signal time behaviour can be given in the terms of the offresonance frequency distribution. If diffusion around the field inhomogeneity as well as intrinsic T_2-relaxation can be neglected, this offresonance frequency distribution corresponds to the Fourier transformation of the time evolution of the magnetization. For more sophisticated sequences as for example SSFP or TrueFISP the signal depends on the distribution of the offresonant spins in a complex manner [8-11]. It was shown that the offresonance frequency distribution around field inhomogeneities can take complicated forms deviating significantly from a Lorentzian or Gaussian shape [12-14]. Thus, the time evolution of the magnetization also deviated significantly from a single exponential decay. For this reason it is necessary to describe the offresonance distribution and therefore the signal evolution properly to obtain correct information about tissue properties from the data measured in an experiment. While the dependence of the frequency distribution on the shape of the

* Corresponding author at: German Cancer Research Center, Radiology, Im Neuenheimer Feld 280, Heidelberg D-69120, Germany.
E-mail address: c.ziener@dkfz-heidelberg.de (C.H. Ziener).

https://doi.org/10.1016/j.mri.2018.09.012
Received 9 June 2018; Received in revised form 10 September 2018; Accepted 13 September 2018

magnetic inhomogeneity and shape of the voxel [2,3,15] as well as the influence of diffusion [16-18] has been studied extensively, the voxel orientation in reference to the external magnetic field has not been studied yet.

In this work, the dependence of the frequency distribution on the voxel orientation in the case of cubic voxels is investigated and the influence on the T_2' relaxation time is demonstrated. For this purpose, an analytic expression of the frequency distribution of a straight vessel in a cubic voxel is derived and compared with numerical simulations and analytical results in the case of a coaxial cylindrical voxel. The obtained frequency distributions $p(\omega)$ are compared with phantom measurements for different voxel orientations. The results can be used to determine blood oxygenation levels from *in vivo* measurements of large veins as experimentally shown in [3] and [19].

2. Methods

In this section, we outline the calculation of the frequency distribution as well as the calculation of the magnetization. The magnetic field around a vessel is given by

$$B(\mathbf{r}) = B_0 \frac{\Delta\chi}{2} \sin^2(\theta) R^2 \frac{\cos(2\phi)}{r^2} , \tag{1}$$

where $\Delta\chi$ is the susceptibility difference between the vessel and the surrounding tissue, B_0 is the external magnetic field, R is the radius of the vessel, θ is the angle between the vessel axis and the external magnetic field, ϕ is the angle in polar coordinates in a cross section perpendicular to the cylinder axis and r is the distance from the center of the vessel in the same cross section (cf. Fig. 1). Using the Larmor relation it is possible to write Eq. (1) in the form

$$\omega(\mathbf{r}) = \delta\omega R^2 \frac{\cos(2\phi)}{r^2} . \tag{2}$$

The position vector in the dephasing volume is given in polar coordinates: $\mathbf{r} = (r,\phi)$. Assuming a homogeneously magnetized vessel, the strength $\delta\omega$ of the dipole field can be obtained as

$$\delta\omega = \gamma B_0 \frac{\Delta\chi}{2} \sin^2(\theta) . \tag{3}$$

The dipole field strength $\delta\omega$ is the characteristic equatorial frequency shift $\delta\omega = \omega(r = R,\phi = 0)$. The signal evolution $S(t)$ for negligible diffusion and constant spin density is given as

$$S(t) = S_0 e^{-\frac{t}{T_2}} \underbrace{\frac{1}{V} \int_V d^2\mathbf{r} e^{-i\omega(\mathbf{r})t}}_{M(t)} . \tag{4}$$

The magnetization $M(t)$ excludes the intrinsic T_2-relaxation mechanism and is normalized to $M(0) = 1$. The frequency distribution $p(\omega)$ is defined as Fourier transform of the magnetization $M(t)$:

$$p(\omega) = \frac{1}{2\pi} \int_{-\infty}^{\infty} dt M(t) e^{i\omega t} . \tag{5}$$

Thus, the frequency distribution $p(\omega)$ is given as

$$p(\omega) = \frac{1}{V} \int_V d^2\mathbf{r} \delta(\omega - \omega(\mathbf{r})) , \tag{6}$$

where V is the volume containing all spins contributing to the signal and δ is the Dirac generalized function. The volume V is determined by the space between the vessel and the voxel boundary and will be referred as dephasing volume, see Fig. 1. Thus, the frequency distribution can be found as histogram over the local Larmor frequency in the measured volume. Under the assumption of a monoexponential decay of the transverse magnetization $M(t)$, the transverse relaxation time T_2' can be calculated with a mean relaxation time approach [20]:

$$T_2' = \int_0^{\infty} dt M(t) . \tag{7}$$

For symmetric frequency distributions $p(-\omega) = p(+\omega)$ that, indeed, is fulfilled for centered vessels as shown later, the transverse relaxation time can be expressed in terms of the frequency distribution (see Eq. (19) in [21]):

$$T_2' = \pi p(\omega = 0) . \tag{8}$$

2.1. Cylindrical voxel boundaries

In 1919, Krogh developed a model, where a cylindrical vessel with radius R is surrounded by a concentric cylindrical voxel with radius R_D, to describe oxygen supply of the tissue [22]. This model has been adapted to the analysis of dephasing in MRI and is in detail studied in the literature [1,23-25]. The volume, where dephasing of spins takes place, is gives as $V = \pi[R_D^2 - R^2]$, see Fig. 1. The outer radius R_D is chosen in a way, that the regional blood volume (RBV = η) remains constant:

$$\eta = \frac{R^2}{R_D^2} . \tag{9}$$

The frequency distribution in Krogh's vessel model can be found as [26]

$$p_{cyl}(\omega) = \frac{\eta}{1-\eta} \frac{\delta\omega}{\pi\omega^2} \times \begin{cases} \sqrt{1 - \left[\frac{\omega}{\delta\omega}\right]^2} - \sqrt{1 - \left[\frac{\omega}{\eta\,\delta\omega}\right]^2} & \text{for } |\omega| < \eta\delta\omega \\ \sqrt{1 - \left[\frac{\omega}{\delta\omega}\right]^2} & \text{for } \eta\delta\omega \le |\omega| < \delta\omega \\ 0 & \text{for } \delta\omega \le |\omega| . \end{cases} \tag{10}$$

The frequency distribution exhibits two prominent peaks at $\omega = -\eta\delta\omega$ and $\omega = +\eta\delta\omega$. Furthermore, it is symmetric $p_{cyl}(+\omega) = p_{cyl}(-\omega)$. Applying Eq. (8), the relaxation time T_2' can be obtained as

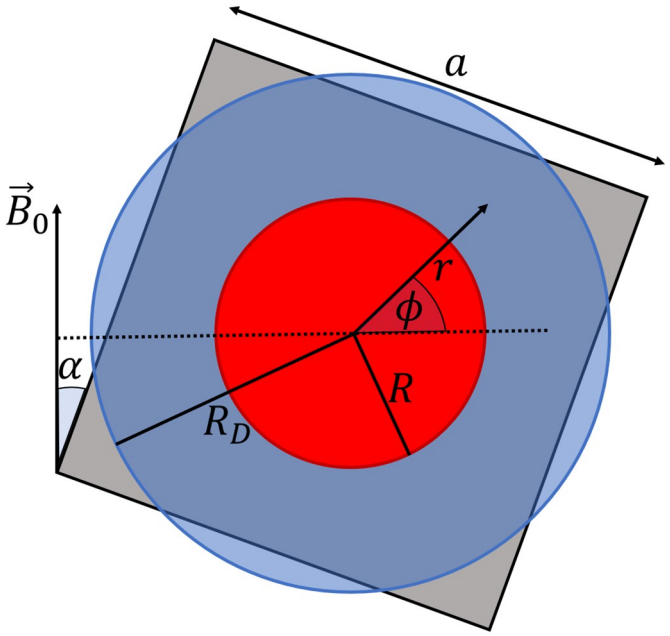

Fig. 1. Cylindrical voxel model vs. cubic voxel model. In the cylindrical voxel model, the vessel with radius R shown in red is surrounded by a concentric cylinder shown in blue. In the cubic voxel model, a quadratic voxel with side length a surrounds the vessel. The results in this model depend on the angle α between magnetic field and voxel orientation. (For interpretation of the references to color in this figure legend, the reader is referred to the web version of this article.)

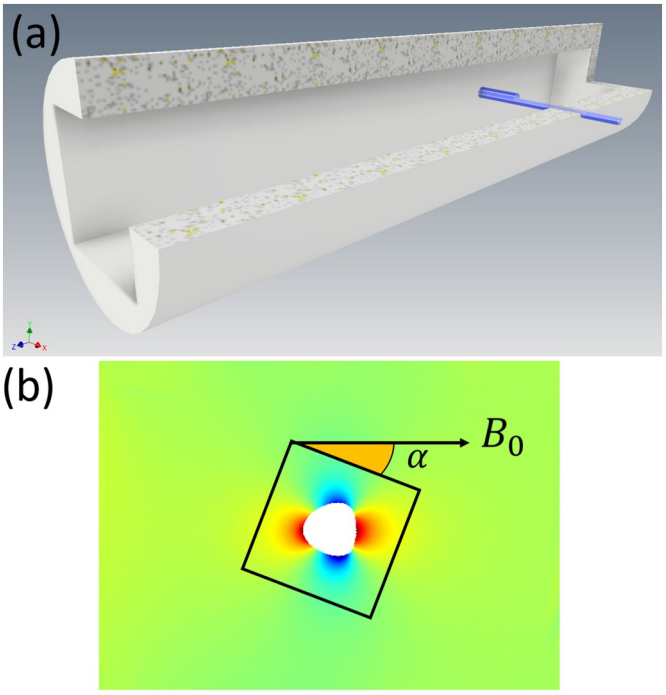

Fig. 2. (a) Phantom and (b) corresponding Larmor frequency map. The outer cylinder has a diameter of 34 mm with a quadratic cavity with edge length of 20 mm. The vessel has an outer diameter of 3 mm and an inner cavity of 2.4 mm. The black square in (b) shows a virtual voxel with side length $a = 6.8$ mm for an arbitrary angle α between voxel orientation and main magnetic field. The volume fraction was chosen as $\eta = 0.15$.

$$T'_{2\mathrm{cyl}} = \frac{1+\eta}{2\eta\delta\omega}\,. \tag{11}$$

2.2. Phantom experiments

A phantom experiment was performed to validate the theoretical results. The phantom was CAD designed (Inventor, Autodesk, USA) and manufactured using FDM (fused deposition modeling) 3D printing method (Raise N2, USA). The phantom consists of a cylinder with an inner cuboid cavity with an axial length of 140 mm and an in plane side length of 19.4 mm. Two holes where placed 40 mm above the bottom of the cylinder perpendicular to two opposite sides of the cavity and perpendicular to the axis of the outer cylinder. Through these holes an air filled hollow glass capillary (305-PS-7, Wilmad-LabGlass, Vineland, NJ, USA) with an outer diameter of $2R_o = 3$ mm and an inner diameter of $2R_i = 2.4$ mm was guided and the bore sealed waterproof. An image of the phantom is shown in Fig. 2 (a). The printing parameter (slice thickness: 100 µm, fill factor: 100%, printing speed: 3600 mm/min, temperature: 225 °C, bed temperature: 40 °C) were optimized to generate a waterproof phantom using PLA material (polylactic acid, Polymaker Polymax PLA [gray], USA). Experiments were conducted on a 7 T horizontal bore small animal scanner (Bruker Biospin, Ettlingen, Germany). The printed phantom was filled with tap water, sealed and carefully placed in the center of the scanner. The cylinder axis was aligned with the external magnetic field and the magnetic field was carefully shimmed to minimize inhomogeneities not associated with the capillary. To calculate field maps 2D FLASH images were acquired in a plane perpendicular to the capillary (TE = 5.8/6.8 ms, TR = 100 ms, FA = 30°, MTX = 1024 × 512, in plane resolution: 50 µm × 50 µm, bandwidth 150 Hz per pixel, slice thickness 3 mm, NA = 64). The phase of the images at the two echo times was subtracted pixelwise and divided by the echo time difference to create a Larmor frequency map. Phase unwrapping was performed based on an algorithm presented in [27]. The phase map is shown in Fig. 2 (b).

Virtual voxels were carefully placed around the center of the vessel with an angle α towards the direction of the main magnetic field as schematically visualized in Fig. 1 and shown in Fig. 2 for the phantom measurements. The Larmor frequency map was used to calculate the frequency distributions as histogram over the virtual voxels for different angles α.

To investigate the influence of the voxel orientation, a single voxel spectroscopy was performed. In this work a semiLASER sequence was used [28]. This sequence is similar to the PRESS sequence [29], but uses pairs of adiabatic refocussing pulses to achieve superior spatial localization. Sequence parameters were TR = 2500 ms, TE = 30 ms, bandwidth ≈4 kHz, spectral resolution ≈2 Hz. The voxel side length in plane was $a = 6.8$ mm and slice thickness was 3 mm. The voxel was centered around the capillary and orientation angle α was varied between 0° and 45° in steps of 5°. The free induction decay was acquired for 512 ms and Fourier transformed to yield the frequency distribution.

3. Results

In this section, the frequency distribution for a cubic voxel is analytically analyzed for arbitrary voxel orientation α and compared with phantom measurements as well as *in vivo* measurements. Due to the symmetry of the cubic voxel, the voxel orientation is restricted to the regime $0° \leq \alpha \leq 45°$ throughout this work.

3.1. Cubic voxel boundaries

Usually in MR experiments the free induction decay is analyzed in a cubic voxel with side length a. Thus, the according line shape of the frequency distribution $p_{\mathrm{cub}}(\alpha,\omega)$ changes significantly compared to Krogh's model [30]. In this model the regional blood volume RBV = η is given as

$$\eta = \frac{\pi R^2}{a^2}\,. \tag{12}$$

In the following it will be assumed that the volume fraction fulfils the relation $\eta < \pi/4 \approx 0.785$. This guarantees that the vessel always fits inside the quadratic voxel. For volume fractions above this critical value it is not possible that the vessel lies entirely within the cubic voxel. As detailed in Appendix A, we provide the first analytic expression for the frequency distribution $p_{\mathrm{cub}}(\alpha,\omega)$ in a voxel:

$$p_{\mathrm{cub}}(\alpha,\omega) = \frac{\eta}{1-\eta}\frac{\delta\omega}{\pi\omega^2}\times \begin{cases} 0 & \text{for } \delta\omega \leq |\omega| \\ \sqrt{1-\left[\frac{\omega}{\delta\omega}\right]^2} & \text{for } \frac{4}{\pi}\eta\delta\omega\cos^3\left(\frac{2\alpha}{3}\right) \\ & \quad \leq |\omega| < \delta\omega \\ \sqrt{1-\left[\frac{\omega}{\delta\omega}\right]^2} & \text{for } |\omega| < \frac{4}{\pi}\eta\delta\omega\cos^3\left(\frac{2\alpha}{3}\right). \\ \quad + \frac{1}{2}\sum_{k=0}^{3}[-1]^k\sin(2\phi_k) & \end{cases} \tag{13}$$

The angles ϕ_k (k = 0,1,2,3) depend on the voxel orientation α and the parameter $|\omega|/[\eta\delta\omega]$. They are ordered $\phi_0 < \phi_1 < \phi_2 < \phi_3$ and obtained as zeros of the function $g(\phi_k) = 0$:

$$g(\phi) = \frac{\pi}{4}\frac{|\omega|}{\eta\delta\omega} - \cos(2\phi)\times \begin{cases} \sin^2(\phi-\alpha) & \text{for } -\frac{\pi}{4} < \phi < \alpha - \frac{\pi}{4} \\ \cos^2(\phi-\alpha) & \text{for } \alpha - \frac{\pi}{4} \leq \phi < +\frac{\pi}{4}. \end{cases} \tag{14}$$

The function g exhibits 0, 2 or 4 zeros in dependence on the parameters

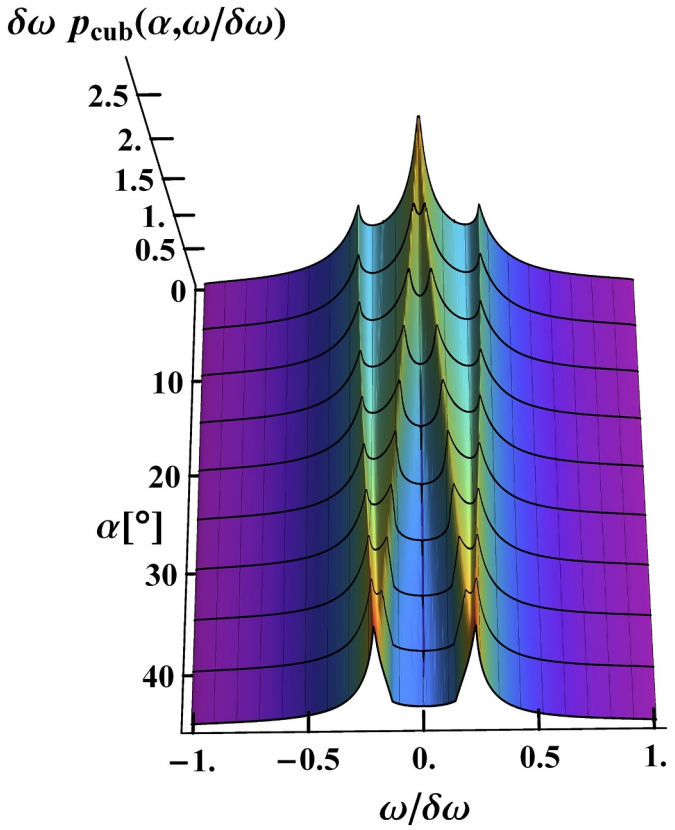

Fig. 3. Frequency distribution $p_{\mathrm{cub}}(\alpha,\omega)$ in dependence on the angle α obtained from Eq. (13) for $\eta = 0.2$. For an alignment of magnetic field B_0 and voxel orientation, $\alpha = 0^\circ$, three peaks occur in the frequency distribution. With increasing angle α, four peaks exist, while in the limiting regime $\alpha = 45^\circ$, only two peaks occur. The peak positions are analyzed in Eq. (19) for the symmetric outer peaks and in Eq. (20) for the symmetric inner peaks. The peak height of the outer peaks given in Eq. (21) increases with increasing angles α, whereas the peak height of the inner peaks decreases.

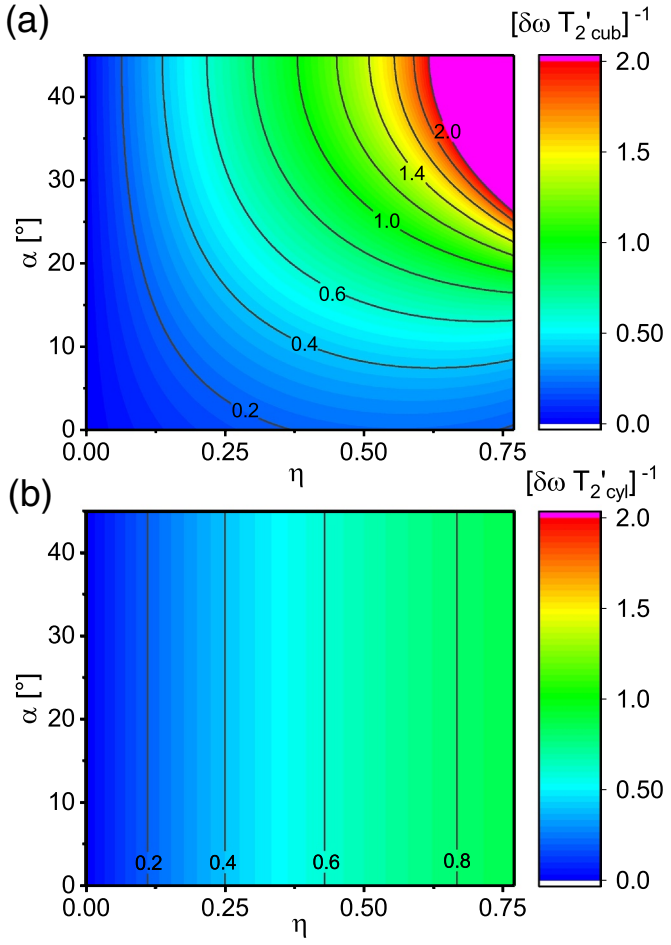

Fig. 4. (a) $1/T'_{2\mathrm{cub}}$ and (b) $1/T'_{2\mathrm{cyl}}$ in dependence on the volume fraction η and the angle α. For small volume fractions $\eta \ll 1$, the ratio between both relaxation times only depends on the angle α, see Eq. (18).

$|\omega|/[\eta\delta\omega]$ and α. Details of the derivation of the frequency distribution are provided in Appendix A.

The frequency distribution is shown in Fig. 3 in the dependence on the angle α that ranges from $0 \le \alpha < \pi/4$ due to the symmetry of the cubic voxel. The relaxation rate T'_2 as defined in Eq. (8) can be obtained as

$$T'_{2\mathrm{cub}} = \frac{\eta}{1-\eta}\frac{1}{2\delta\omega}\left[\left[\frac{\pi}{2\eta[1+\sin(2\alpha)]}\right]^2 - 1\right]. \tag{15}$$

The dependence of T'_2 on the volume fraction η and the angle α is shown in Fig. 4. The strong dependence of T'_2 on the orientation of the voxel is obvious. Ignoring this fact leads to a strong bias in the quantification of the dipole field strength for measured T'_2-values.

With the help of this result it is possible to find the angle α for which the T'_2 relaxation time in the case of a cubic voxel given in Eq. (15) is the same as in the case of a cylindrical voxel given in Eq. (11). After some algebra it is easy to see that this angle is independent of the volume fraction η and given by

$$\frac{\pi}{4} - \arccos\left(\frac{\sqrt{\pi}}{2}\right) \approx 17.4^\circ . \tag{16}$$

For this angle, the frequency distributions are compared in Fig. 5 (b). One clearly sees that at $\omega = 0$ both frequency distributions exhibits the same value.

For $\alpha = 3\arccos(\sqrt[3]{\pi/4})/2 \approx 34.0^\circ$, the outer peaks of the frequency distribution for a cubic voxel coincide with the peaks of the frequency distribution in Krogh's vessel model, see Fig. 5c. Thus, the frequency distribution for the cubic voxel coincides with the frequency distribution of the cylindrical voxel for $|\omega| > 4\eta\delta\omega\cos^3(2\alpha/3)/\pi$ for $\alpha < 3\arccos(\sqrt[3]{\pi/4})/2$. For $\alpha \ge 3\arccos(\sqrt[3]{\pi/4})/2$, both frequency distributions coincide for $|\omega| > \eta\delta\omega$. The frequency distribution and the corresponding voxel geometry are compared in Fig. 5 with the cylindrical voxel model for $\alpha = 0^\circ$, $\alpha = 17.4^\circ$, $\alpha = 34.0^\circ$ and $\alpha = 45^\circ$. Since the volume fraction η is usually very low, it is convenient to analyze the limit $\eta \to 0$. Thus, the relaxation time T'_2 can be found as

$$T'_{2\mathrm{cub}} \approx \frac{1+\eta}{\eta}\frac{\pi^2}{8\delta\omega}\frac{1}{[1+\sin(2\alpha)]^2} . \tag{17}$$

Comparing Eq. (17) with Eq. (11) in the limit of small volume fractions η one can see that the ratio of the relaxation times of the cylindrical and cubic voxel $T'_{2,\mathrm{cyl}}/T'_{2,\mathrm{cub}}$ is only determined by the angle α:

$$\frac{T'_{2,\mathrm{cyl}}}{T'_{2,\mathrm{cub}}} = \frac{4}{\pi^2}[1+\sin(2\alpha)]^2 . \tag{18}$$

For the two limiting cases of $\alpha = 0$ and $\alpha = \pi/4$ this ratio is $4/\pi^2 = 0.405285$ and $16/\pi^2 = 1.62114$, respectively.

As shown in Fig. 3, the frequency distribution $p_{\mathrm{cub}}(\alpha,\omega)$ exhibits three peaks for $\alpha = 0$, two peaks for $\alpha = \pi/4$ and four peaks elsewhere. A detailed analysis of Eq. (13) allows finding the peak positions ω_p:

$$\omega_p^{1,2} = \pm\frac{4}{\pi}\eta\delta\omega\cos^3\left(\frac{2\alpha}{3}\right) \tag{19}$$

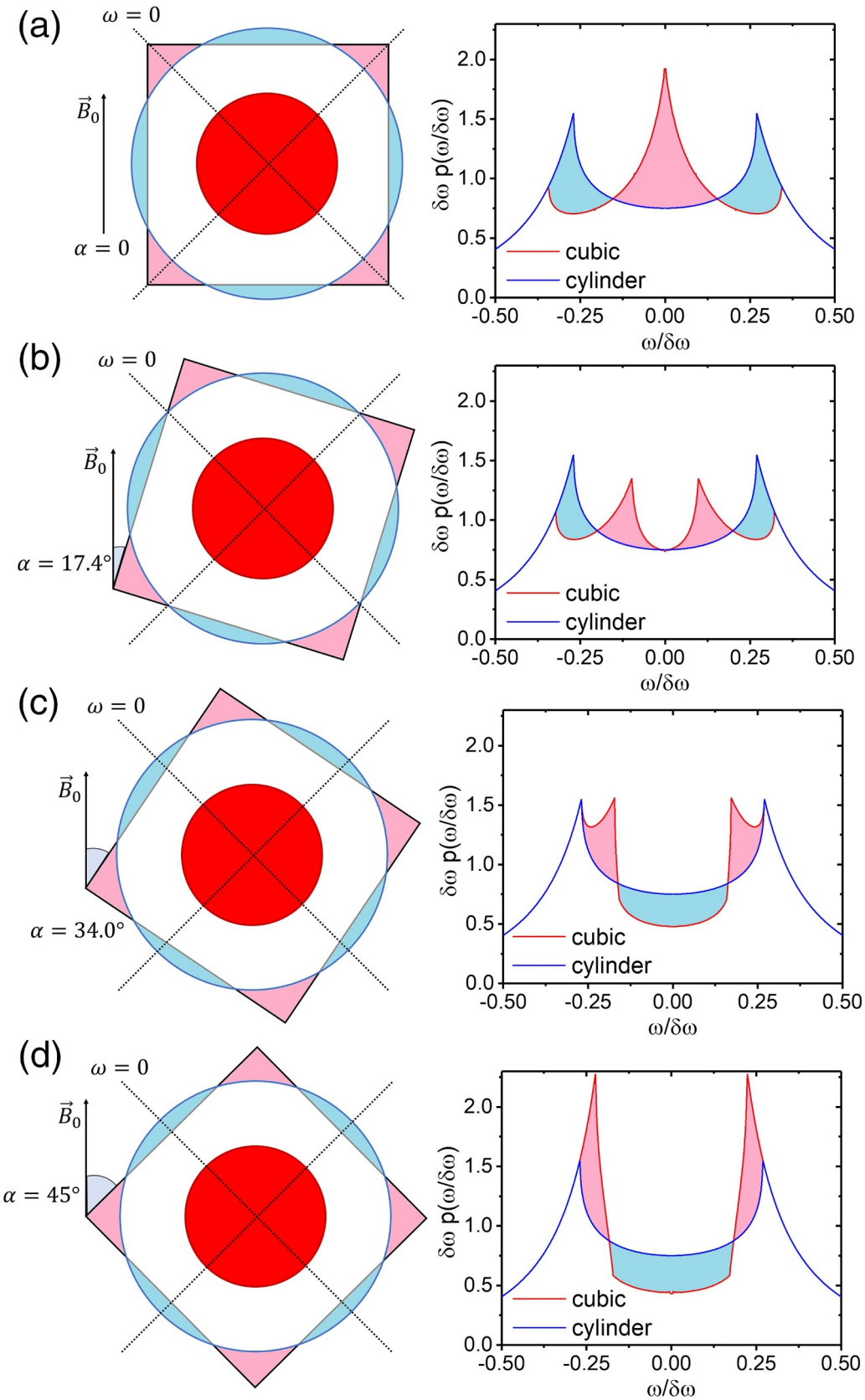

Fig. 5. Comparison of voxel geometry and frequency distribution between cylindrical voxel model (blue lines obtained from Eq. (10)) and cubic voxel model (red lines obtained from Eq. (13)) for (a) $\alpha = 0^\circ$, (b) $\alpha = 17.4^\circ$, (c) $\alpha = 34.0^\circ$ and (d) $\alpha = 45^\circ$. Areas in light blue mark positions that only contribute in the cylindrical model, while areas in light red mark positions that only contribute in the cubic voxel model. The dotted lines in the left half of the figure indicates the positions where the local Larmor frequency is $\omega = 0$. The length of these lines inside the voxels is relevant for calculation of the T_2' relaxation time in the mean relaxation time approach, see Eq. (7). Thus, T_2' is increased in the cubic model for $\alpha = 0^\circ$, equal for $\alpha = 17.4^\circ$ and smaller for $\alpha = 34.0^\circ$ and $\alpha = 45^\circ$ compared to the cylindrical model. The peak position is shown in Fig. 6. (For interpretation of the references to color in this figure legend, the reader is referred to the web version of this article.)

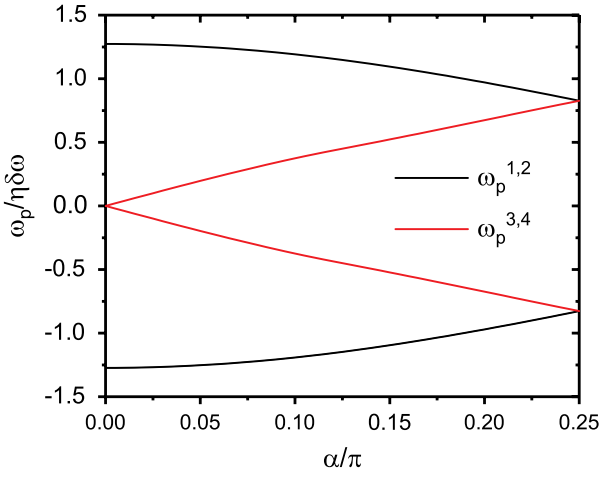

Fig. 6. Position ω_p of the peaks in the frequency distribution in dependence on the angle α. The peak positions are given in Eqs. (19) and (20). In the limits $\alpha = 0$, three peaks occur at positions $\omega_p^{1,2} = \pm 4\eta\delta\omega/\pi$ and $\omega_p^3 = 0$, while two peaks occur in opposite limit $\alpha = \pi/4$ at positions $\omega_p^{1,2} = \pm 3\sqrt{3}\eta\delta\omega/[2\pi]$. For different angles α, the frequency distribution exhibits four peaks.

$$\omega_p^{3,4} = \pm\frac{2}{\pi}\eta\delta\omega\begin{cases}\sin(2\alpha) & \text{for } 0 \le \alpha \le \pi/8\\ 2\sin^3\left(\frac{2\alpha}{3}+\frac{\pi}{6}\right) & \text{for } \pi/8 < \alpha \le \pi/4\end{cases}. \tag{20}$$

The peak positions in dependence on the angle α are shown in Fig. 6. The frequency distribution at the outer peaks takes the value

$$p(\omega_p^{1,2}) = \frac{\sqrt{\pi^2 - 16\eta^2\cos^6\left(\frac{2\alpha}{3}\right)}}{\eta[1-\eta]\delta\omega\cos^6\left(\frac{2\alpha}{3}\right)}. \tag{21}$$

Obviously, the outer peaks increase with increasing angle α as shown in Fig. 3. The width $\langle\omega^2\rangle$ of the frequency distribution as defined in Eq. (44) in Appendix A can be obtained as

$$\langle\omega^2\rangle = \frac{\eta}{1-\eta}\delta\omega^2\left[\frac{1}{2}+\frac{2\eta}{\pi}\left[\frac{1}{\pi}-2-\frac{1}{3\pi}\cos(4\alpha)\right]\right]. \tag{22}$$

3.2. Phantom experiments

For a validation of the theoretical findings, phantom measurements were performed as described above. The dipole field strength $\delta\omega$ was obtained from the phase shift at the boundary of the vessel between the two echo times resulting in a dipole field strength of $\delta\omega \approx 5500\ \mathrm{s}^{-1}$. This value is close to the expected value assuming a susceptibility difference between air and water of 8–9 ppm [6,31] and the gyromagnetic ratio $\gamma = 2\pi \times 42.6\ \mathrm{MHz\ T}^{-1}$ [32]. The dipole field strength decreases with the inverse quadratic distance and, thus, the ratio between inner ($R_i = 1.2$ mm) and outer radius ($R_o = 1.5$ mm) of the vessel needs to be accounted. Finally, one obtains the expected dipole field strength as

$$\delta\omega = \gamma B_0\frac{\Delta\chi}{2}\frac{R_i^2}{R_o^2} \approx 5300\ \mathrm{s}^{-1}. \tag{23}$$

The frequency distribution $p_{\mathrm{cub}}(\alpha,\omega)$ was obtained from virtual voxels that were selected from the field map. Moreover, a semiLASER sequence was used to obtain spectroscopic measurements. A comparison between measured and theoretical frequency distributions is shown in Fig. 7 for different angles α and a blood volume fraction of $\eta = 0.15$. The theoretical frequency distribution was calculated assuming $\delta\omega = 5500\ \mathrm{s}^{-1}$. Theoretical and experimental frequency distributions agree very well. The peak structure of the frequency distribution based on virtual voxels is close to the expected peak structure with three peaks for $\alpha = 0°$, two peaks for $\alpha = 45°$ and four peaks elsewhere. The relaxation time T_2' is obtained from the semiLASER measurement in dependence on the angle α according to Eq. (7). The results are shown in Fig. 8 and show very well the functional dependence that is theoretical predicted by Eq. (15). However, since the measured frequency distribution is smeared out compared to the theoretical frequency distribution, a shorter T_2'-relaxation time is measured than expected and, thus, the obtained dipole field strength $\delta\omega \approx 6800\ \mathrm{s}^{-1}$ is slightly overestimated as shown in Fig. 8. This may be avoided by using the peak distance for $\alpha = 45°$ that is given by Eq. (19):

$$\delta\omega = \pi\frac{\omega_p^2 - \omega_p^1}{3\eta\sqrt{3}} \approx 6000\ \mathrm{s}^{-1}, \tag{24}$$

where the measured peak distance from Fig. 7 (d) was used.

3.3. In vivo application

The developed theory can be applied to analyze the blood oxygenation of single vessels, *e.g.* veins in the brain as demonstrated by Sedlacik et al. [3,19]. There, the *V. centralis*, which is parallel to the magnetic field ($\theta = 0°$), and the *V. thalamostriata*, which is perpendicular to the main magnetic field ($\theta = 90°$) were analyzed and measurements were compared with numerical simulations of the frequency distribution and corresponding free induction decay. However, those works were restricted to the case of $\alpha = 0°$. To compare the theoretical free induction decay with measurements, one needs to account for the MR signal contribution of the blood-filled vessel as well as the intrinsic T_2-effects. The contribution of the blood-filled vessels oscillates with the frequency $-\delta\omega[\cos^2(\theta) - 1/3]$ as discussed *e.g.* in [19] and [33]. Finally, the signal reads

$$\frac{S(t)}{S_0} = [1-\eta]M(0,t)\mathrm{e}^{-\frac{t}{T_{2,\mathrm{tis}}}} + \eta\mathrm{e}^{-\frac{t}{T_{2,\mathrm{blo}}}}\mathrm{e}^{-\mathrm{i}\delta\omega t\left[\cos^2(\theta)-\frac{1}{3}\right]}, \tag{25}$$

where the magnetization $M(0,t)$ with $\alpha = 0°$ is given in Eq. (48) in Appendix A and $T_{2,\mathrm{tis}}$ and $T_{2,\mathrm{blo}}$ are the intrinsic relaxation times for tissue and blood, respectively. The size of the measured veins was approximatively $R \approx 0.6$–1.4 mm and the voxel size was $a = 3$ mm, resulting in a blood volume fraction in the range of $\eta = 0.1$–0.7, see Table 1 in [19]. The dipole field strength $\delta\omega$ as defined in Eq. (3) depends on the susceptibility difference $\Delta\chi$ between blood and tissue:

$$\Delta\chi = \chi_{do}\,\mathrm{Hct}[1-Y], \tag{26}$$

where $\chi_{do} = 3.39$ ppm is the susceptibility difference between oxygenated and deoxygenated blood that agrees with the susceptibility difference between deoxygenated blood and surrounding tissue [34], Hct is blood's hematocrit and the blood oxygenation level is denoted as Y.

We compare the theoretical signal with experimental results from the thalamostriate vein obtained by Sedlacik et al. [3]. Therefore, we used the relaxation times $T_{2,\mathrm{tis}} = 86$ ms and $T_{2,\mathrm{blo}} = 61$ ms, a volume fraction of $\eta = 0.25$ and a dipole field strength of $\delta\omega = 88.1\ \mathrm{s}^{-1}$ as suggested in [3]. The comparison is shown in Fig. 9. The results agree very well, thus, indicating that the developed theory is applicable for measuring oxygenation levels in large veins.

4. Discussion and Conclusion

In this work the strong dependence of the offresonance frequency distribution $p_{\mathrm{cub}}(\alpha,\omega)$ on the voxel orientation α in an external magnetic field is demonstrated. This leads to a strong variation of the $T_{2,\mathrm{cub}}'$ relaxation time and has to be considered if T_2' is used for quantification. Exploiting the symmetry of the frequency distribution the T_2' relaxation time in the case of a cubic voxel is determined in the sense of a mean relaxation time approximation (see Eq. (7)). This provides the possibility to quantify the influence of orientation and compare it with the other parameters. A simple expression for the T_2' relaxation time is obtained which shows how to scale the parameters without changing

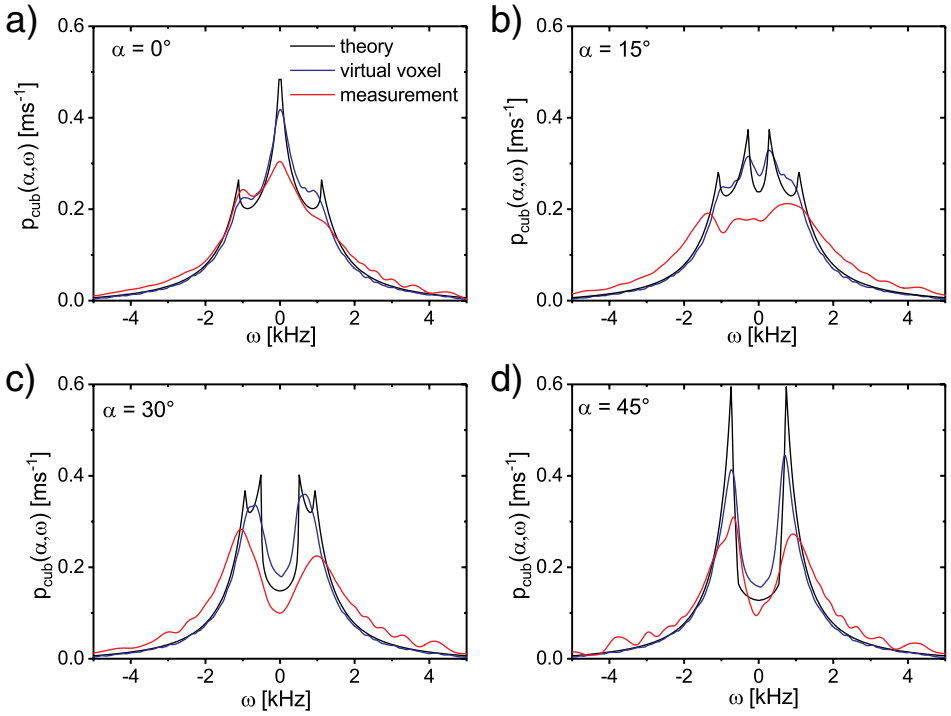

Fig. 7. Comparison of measured and theoretical frequency distributions $p_{cub}(\alpha,\omega)$ in dependence on the angle α. The black lines show theoretical expectations given in Eq. (13) for $\delta\omega = 5500$ s^{-1}. The blue line was obtained from virtual voxels selected in the field map of the phantom. The red line shows measurements with a semi-LASER sequence. The regional blood volume fraction was $\eta = 0.15$. Experimental and theoretical line shapes according to Eq. (13) agree very well to each other and the expected peak structure described by Eqs. (19) and (20) is observed in the experiment. (For interpretation of the references to color in this figure legend, the reader is referred to the web version of this article.)

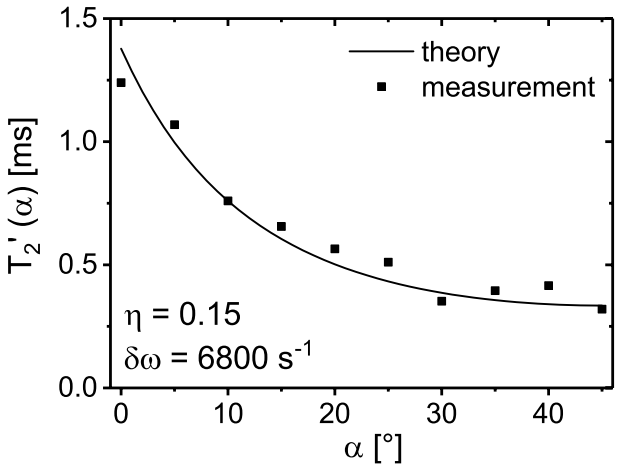

Fig. 8. Angular dependence of the relaxation time T_2' for theoretical and measured free induction decay obtained from a semiLASER sequence. The measurements validate very well the functional dependence of the relaxation time T_2'. Since the measured frequency distribution in Fig. 7 is typically smaller for $\omega = 0$ than the theoretical value, the relaxation times are underestimated in the experiments, see Eq. (8). According to Eq. (15), the fitted dipole field strength $\delta\omega = 6800$ s^{-1} is therefore larger as expected.

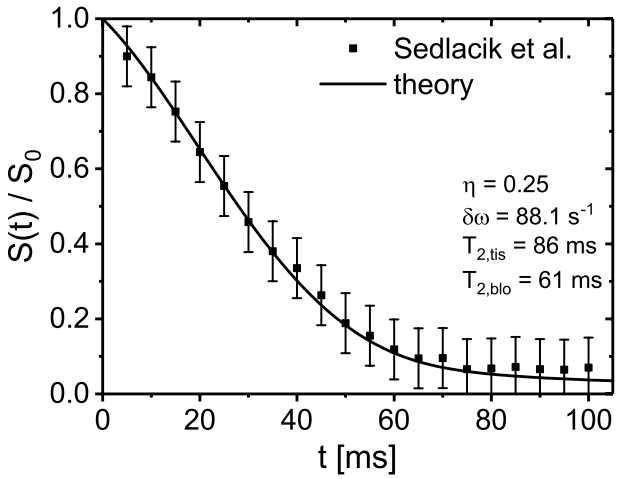

Fig. 9. Comparison between theoretical free induction decay obtained from Eq. (25) and measurements obtained from Sedlacik et al. [3] for *V. thalamostriata* with $\theta = 90°$ and $\alpha = 0°$.

the T_2'. Furthermore, it has been demonstrated that T_2' depends on the angle and differs from the case of a cylindrical voxel with the same volume fraction η even in the case of low regional blood volume fraction $\eta \ll 1$. An interesting fact is that the T_2' relaxation times for a cubic and a cylindrical voxel with the same volume fraction coincide for the angle $\alpha = 17.4092°$ independently from the value of the volume fraction η and the characteristic equatorial frequency shift $\delta\omega$. This demonstrates that this relation is completely determined by the shape of the voxels and not by their size or the strength of the magnetic inhomogeneity.

It is important to note that there is a close connection between the T_2' relaxation time and the frequency distribution. It is clear that the complete frequency distribution contains more detailed information on the geometry than its value for $\omega = 0$. This is comparable to the fact that the complete time evolution of the magnetization provides more information than the simple T_2' relaxation time constant. Thus, it is advantageous to have the full frequency distribution at hand. We first provided an analytic expression for the frequency distribution $p_{cub}(\alpha,\omega)$ in dependence on the angle α and the blood volume fraction η. The analytical expression of the frequency distribution shows a near-perfect agreement with numerical simulations of the same geometrical model for the whole range of the parameters η, α and $\delta\omega$ (not shown in the manuscript). For instance, Fig. 2(b) in [3] agrees with the red line in Fig. 5 (a).

Another reason why the frequency distribution is more useful than the T_2' relaxation time constant is due to the fact that the offresonance frequency distribution around a vessel exhibits either two, three or four peaks (see Figs. 3 and 6) and, thus, a strong non-Lorentzian behaviour. However, a Lorentzian-like shape is necessary to characterize the signal

evolution sufficiently with the help of a single relaxation time. In this situation, the frequency distribution provides a way to obtain more meaningful results from the measurements.

Compared to the previous literature, this work provides the first analytical expressions for the frequency distribution and the free induction decay for this geometry, whereas previous publications are based on numerical simulations or circular geometries [3,19]. Numerical simulations of the free induction decay around a single vein are described in detail in [30]. Moreover, all previous publications neglected the angle α between magnetic field and voxel orientation and focussed on the angle θ between magnetic field and direction of the vessel. However, as shown in this work, the frequency distribution highly depends on this angle α.

The frequency distribution was obtained under the assumption of negligible intrinsic T_2 decay and negligible diffusion. For realistic measurements, however, the intrinsic relaxation may not be negligible and, thus, the frequency distribution will be convolved with a Lorentzian line shape of width T_2. Diffusion effects can be accounted by the strong collision approximation that connects the frequency distribution for arbitrary diffusion effects with the frequency distribution in the static dephasing regime, where diffusion effects are neglected [14,35].

The frequency distribution depends on the position of the voxel, *e.g.* non-centered vessels would lead to changes in the frequency distribution. In general, the frequency distribution becomes asymmetric and, thus, the free induction decay does not necessarily remain real. Since the Larmor frequency is proportional to the inverse quadratic distance $\omega(r,\phi) \propto r^{-2}$, non-centered vessels change only the center of the frequency distribution, where small frequencies are located. While in principle the mathematical analysis presented in this work can also be performed with arbitrary shifted voxels, the obtained mathematical expression of the frequency distribution is equally complicated as its numerical implementation. Thus, we analyzed the frequency distribution for $\alpha = 0^\circ$ for position shifts of the vessels in the y-direction, see Appendix B. As shown in Fig. 11, the frequency distribution is only slightly changed, if the displacement ϵ is small compared to the radius of the vessel ($\epsilon < R/2$) and the peak structure mainly remains unaffected. For larger displacements, however, strong differences in the frequency distribution occur.

Seppenwoolde et al. analyzed the frequency distribution around a sphere in a cubic voxel based on numerical histogram techniques [36]. The three-dimensional dipole field around a sphere has different mathematical properties than the two-dimensional field around a vessel. However, a similar calculation as presented in this work might lead to an analytic expression for the frequency distribution around a sphere as well.

The determined frequency distributions from phantom measurements agree very well with theoretical results. Sources of possible uncertainties arises from non-perfect shimming of the field of view, since long-range magnetic field inhomogeneities should be correctly shimmed but the small-range magnetic field inhomogeneity from the vessel should not be disturbed. As the field map given in Fig. 2 (b) show, however, the frequency distribution is not significantly affected by these deviations.

The obtained frequency distributions and corresponding free induction decays can be used to quantify blood oxygenation levels by measuring the signal evolution around large veins as *e.g.* performed in [3] and [19]. A comparison between measured free induction decay and expected theoretical results shows good agreements (see Fig. 9). For experimental measurements, the intrinsic T_2-relaxation time as well as the signal contribution of blood-filled vessels cannot be neglected and the signal is given by Eq. (25). The intrinsic T_2-effects lead to a convolution of the derived frequency distribution with a Lorentzian line shape, whose width is determined by the T_2-relaxation time. The relaxation time T_2' agrees very well with theoretical expectation, however, the obtained dipole field strength $\delta\omega$ is slightly overestimated since the measured frequency distribution is smeared out compared to the theoretical frequency distribution. Thus, in future works, it may be helpful to perform measurements with angle $\alpha = 45^\circ$ and calculate the dipole field strength by measuring the peak distance as given in Eq. (24), since the distance between the peaks is maximized at this value (see Eq. (19) and Fig. 6) and the peaks are clearly separated (see Eq. (21) and Fig. 5). The contribution of the blood-filled vessels leads to an additional Lorentzian peak in the frequency distribution, whose width is determined by the T_2-relaxation time of the blood. The peak is located around $\omega = -[\cos^2(\theta) - 1/3]\delta\omega$.

The quality of the obtained frequency distributions depends on the spatial localization of the measured voxel and, thus, it is advantageous to use a semiLASER sequence. For other MR imaging sequences, like multi-echo gradient echo sequences, **k**-space data usually are acquired and a discrete Fourier transform leads to the MR image. Thus, the magnetization $M_i(t)$ in voxel with index i is in general not a superposition over the local magnetization inside the voxel i as given in Eq. (4), but given as convolution between local magnetization $m(\mathbf{r},t)$ and point spread function PSF($\mathbf{r}$):

$$M_i(t) = \int_{\mathbb{R}^2} \mathrm{d}^2\mathbf{r}\, m(\mathbf{r}, t)\mathrm{PSF}(\mathbf{r} - \mathbf{r}_i)\,, \tag{27}$$

where $\mathbf{r}_i$ is the position vector to the center of the voxel with index i. For classical Cartesian sampling of the **k**-space, the point spread function is given as $\mathrm{PSF}(\mathbf{r}) = \mathrm{sinc}\left(\frac{x}{\pi a}\right)\mathrm{sinc}\left(\frac{y}{\pi a}\right)\mathrm{sinc}\left(\frac{z}{\pi a}\right)$. This problem can be met *e.g.* by using a Hanning filter [32]. For a robust application of the developed method, it is useful to connect this magnitude-based approach with phase-based approaches [37]. Hereby, the theoretical results for the magnitude might be used as regularization constraint for quantitative susceptibility maps [38].

In this work, only a single macroscopic vessel has been analyzed. The analysis of a large number of microscopic capillaries is more cumbersome [1,39]. A voxel with several vessels for different arrangements has numerically been examined in [18].

Finally, we analyzed the frequency distribution around a single vessel in a cubic voxel for arbitrary angles α between voxel orientation and magnetic field. The peak structure of the frequency distribution characteristically depends on the angle α: for $\alpha = 0^\circ$, three peaks exist, for $\alpha = 45^\circ$ two peaks occur, for other angles α four peaks exist. These results were validated with phantom measurements. The implementation of the analytic solution is much faster and more precise than numerical simulations and, thus, the results are relevant for the quantitative analysis of macroscopic vessels.

Acknowledgements

We thank Jan Sedlacik for providing data of their experimental *in vivo* measurements. Helpful discussions with Jan Sedlacik and Simon Triphan are gratefully acknowledged. This work was supported by grants from the Deutsche Forschungsgemeinschaft (Contract Grant numbers: DFG ZI 1295/2-1 and DFG KU 3555/1-1). L. R. Buschle was supported by Studienstiftung des deutschen Volkes.

Appendix A. Derivation of the frequency distribution $p_{\mathrm{cub}}(\alpha,\omega)$

As shown in Eq. (4) the free induction decay is a superposition of the local magnetization $m(\mathbf{r},t)$ over the dephasing volume V. Thus, the frequency distribution can be separated in two parts:

$$p_{\mathrm{cub}}(\alpha,\omega) = p_{\tilde{V}}(\alpha,\omega) - p_{V_0}(\omega) \tag{28}$$

$$= \frac{1}{\pi V}\mathrm{Re}\left(\int_0^{+\infty} \mathrm{d}t\ \mathrm{e}^{-\mathrm{i}\omega t}\left[\int_{\tilde{V}} \mathrm{d}^2\mathbf{r}\ m(\mathbf{r},t) - \int_{V_0} \mathrm{d}^2\mathbf{r}\ m(\mathbf{r},t)\right]\right), \tag{29}$$

where $\tilde{V} = a^2$ is the total voxel inclusive the volume of the cylinder and $V_0 = \pi R^2$ is the volume of the cylinder, i.e. $V = \tilde{V} - V_0 = a^2 - \pi R^2$ (red circle in Fig. 1). The contribution $p_{V_0}(\omega)$ of the cylinder can easily be evaluated in polar coordinates using Eq. (4) and the Fourier transform defined in Eq. (5):

$$p_{V_0}(\omega) = \frac{1}{2\pi}\frac{1}{V}\int_{-\infty}^{+\infty} \mathrm{d}t\ \mathrm{e}^{-\mathrm{i}\omega t}\int_0^R \mathrm{d}r r\int_0^{2\pi} \mathrm{d}\phi\ \mathrm{e}^{\mathrm{i}\delta\omega t R^2\frac{\cos(2\phi)}{r^2}} \tag{30}$$

$$= \frac{1}{V}\int_0^R \mathrm{d}r r\int_{-\infty}^{+\infty} \mathrm{d}t \mathrm{e}^{-\mathrm{i}\omega t} J_0\left(\delta\omega\frac{R^2}{r^2}t\right) \tag{31}$$

$$= \frac{2}{V}\int_0^{\min\left\{R\sqrt{\frac{\delta\omega}{\omega}},R\right\}} \mathrm{d}r\frac{r^3}{\sqrt{R^4\delta\omega^2 - r^4\omega^2}} \tag{32}$$

$$= \begin{cases} \dfrac{\eta}{1-\eta}\dfrac{\delta\omega}{\pi\omega^2} & \text{for } |\omega| > \delta\omega \\ \dfrac{\eta}{1-\eta}\dfrac{\delta\omega}{\pi\omega^2}\left[1 - \sqrt{1 - \left[\dfrac{\omega}{\delta\omega}\right]^2}\right] & \text{for } |\omega| < \delta\omega\ . \end{cases} \tag{33}$$

The contribution from the volume $\tilde{V}$ is calculated with Eq. (6). We consider $\omega > 0$. The frequency distribution can then be obtained from the symmetry relation $p_{\mathrm{cub}}(\alpha,+\omega) = p_{\mathrm{cub}}(\alpha,-\omega)$. In general, the outer contribution to the frequency distribution reads

$$p_{\tilde{V}}(\alpha,\omega) = \frac{4}{V}\left[\int_{-\frac{\pi}{4}}^{\alpha-\frac{\pi}{4}} \mathrm{d}\phi \int_0^{\frac{a}{2\sin(\alpha-\phi)}} \mathrm{d}r r + \int_{\alpha-\frac{\pi}{4}}^{+\frac{\pi}{4}} \mathrm{d}\phi \int_0^{\frac{a}{2\cos(\phi-\alpha)}} \mathrm{d}r r\right]\delta\left(\underbrace{\omega - \delta\omega R^2\frac{\cos(2\phi)}{r^2}}_{=q(r)}\right). \tag{34}$$

To evaluate the Dirac distribution, it is advantageous to define the argument of the Dirac distribution as the function $q(r) = \omega - \delta\omega R^2\cos^2(\phi)/r^2$. This function exhibits only one single zero

$$r_0 = R\sqrt{\frac{\delta\omega}{\omega}\cos(2\phi)}\ , \tag{35}$$

and, therefore, the Dirac distribution can be written as

$$\delta(q(r)) = \frac{\delta(r-r_0)}{|q'(r_0)|}\ , \tag{36}$$

where $q(r_0) = 0$. We use Eq. (36) to evaluate the radial integral in Eq. (34). Since the radius r is a real quantity, we can focus on $-\pi/4 \le \phi \le +\pi/4$:

$$p_{\tilde{V}}(\alpha,\omega) = \frac{4}{V}\left[\int_{-\frac{\pi}{4}}^{\alpha-\frac{\pi}{4}} \mathrm{d}\phi \int_0^{\frac{a}{2\sin(\alpha-\phi)}} \mathrm{d}r + \int_{\alpha-\frac{\pi}{4}}^{+\frac{\pi}{4}} \mathrm{d}\phi \int_0^{\frac{a}{2\cos(\phi-\alpha)}} \mathrm{d}r\right]\delta\left(r - R\sqrt{\frac{\delta\omega}{\omega}\cos(2\phi)}\right)\frac{r^4}{R^2\delta\omega\cos(2\phi)}\ . \tag{37}$$

The delta distribution does only contribute, if its argument is inside the integral boundaries. Thus, we get the conditions

$$\sin^2(\phi-\alpha)\cos(2\phi) < \frac{a^2}{4R^2}\frac{\omega}{\delta\omega} \tag{38}$$

$$\cos^2(\phi-\alpha)\cos(2\phi) < \frac{a^2}{4R^2}\frac{\omega}{\delta\omega}\ , \tag{39}$$

for the first and second integral, respectively. Finally, one can rewrite the outer frequency distribution:

$$p_{\tilde{V}}(\alpha,\omega) = \frac{1}{\pi}\frac{\eta}{1-\eta}\frac{\delta\omega}{\omega^2}f(\alpha,\omega)\ , \tag{40}$$

with

$$f(\alpha,\omega) = \int_{-\frac{\pi}{4}}^{\alpha-\frac{\pi}{4}} \mathrm{d}\phi\cos(2\phi)\Theta\left(\frac{\pi}{4}\frac{|\omega|}{\eta\delta\omega} - \sin^2(\phi-\alpha)\cos(2\phi)\right) + \int_{\alpha-\frac{\pi}{4}}^{+\frac{\pi}{4}} \mathrm{d}\phi\cos(2\phi)\Theta\left(\frac{\pi}{4}\frac{|\omega|}{\eta\delta\omega} - \cos^2(\phi-\alpha)\cos(2\phi)\right). \tag{41}$$

The Heaviside-function is denoted as Θ. For $\frac{4}{\pi}\cos^3\left(\frac{2\alpha}{3}\right)\eta\delta\omega < |\omega| < \frac{4}{\pi}\eta\delta\omega$ one finds that $f(\alpha,\omega) = 1$. Finally, we arrive at

$$p_{\mathrm{cub}}(\alpha,\omega)=\frac{\eta}{1-\eta}\frac{\delta\omega}{\pi\omega^2}\times\begin{cases}0 & \text{for } \delta\omega\le|\omega|\\ \sqrt{1-\dfrac{\omega^2}{\delta\omega^2}} & \text{for } \dfrac{4}{\pi}\cos^3\left(\dfrac{2\alpha}{3}\right)\eta\delta\omega\le|\omega|<\delta\omega\\ \sqrt{1-\dfrac{\omega^2}{\delta\omega^2}}+f(\alpha,\omega)-1 & \text{for } |\omega|<\dfrac{4}{\pi}\cos^3\left(\dfrac{2\alpha}{3}\right)\eta\delta\omega\ .\end{cases}\tag{42}$$

In general, the integral in the $f(\alpha,\omega)$-function can be evaluated by finding the zeros of the argument of the Heaviside-function. Thus, the argument of the Heaviside-function is defined as $g(\phi)$ and Eq. (14). Finally, one obtains the frequency distribution as given Eq. (13) that depend on the zeros ϕ_k. The zeros ϕ_k can *e.g.* be obtained in MATHEMATICA® (WolframResearch, Inc., Champaign, IL, USA) as

```
alpha = Pi/6;
eta = 0.1;
deltaomega = 1;
omega = 0.1;
x = Abs[omega]/eta/deltaomega;
phi[k_]=Sort[Join[
  Select[phi/.NSolve[Pi/4*x - Cos[phi-alpha]^2*Cos[2phi], phi, Reals]
    /. C[1] -> 0, (-Pi/4 + alpha < # < +Pi/4) &],
  Select[phi/.NSolve[Pi/4*x - Sin[phi-alpha]^2*Cos[2phi], phi, Reals]
    /. C[1] -> 0, (-Pi/4 < # < -Pi/4 + alpha) &]
]][[k]];
```

In the case of $\alpha=0$, the frequency distribution $p_{\mathrm{cub}}(0,\omega)$ can be obtained as

$$p_{\mathrm{cub}}(0,\omega)=\frac{1}{\pi}\frac{\eta}{1-\eta}\frac{\delta\omega}{\omega^2}\begin{cases}0 & \text{for } \delta\omega<|\omega|\\ \sqrt{1-\dfrac{\omega^2}{\delta\omega^2}} & \text{for } \dfrac{4}{\pi}\eta\delta\omega<|\omega|<\delta\omega\\ \sqrt{1-\dfrac{\omega^2}{\delta\omega^2}}-\sqrt{\dfrac{1}{2}-\dfrac{\pi}{2\eta}\dfrac{\omega}{\delta\omega}+\dfrac{1}{2}\sqrt{1+\dfrac{2\pi}{\eta}\dfrac{\omega}{\delta\omega}}} & \text{for } 0<|\omega|<\dfrac{4}{\pi}\eta\delta\omega\ ,\end{cases}\tag{43}$$

where we used the relation $\sin(2\arccos(x))=2x\sqrt{1-x^2}$. The width $\langle\omega^2\rangle$ of the frequency distribution is defined as

$$\langle\omega^2\rangle=\int_{-\infty}^{\infty}\mathrm{d}\omega\omega^2 p(\omega)\ .\tag{44}$$

Inserting Eq. (13) into Eq. (44), one might arrive at

$$\langle\omega^2\rangle=\frac{2\eta}{1-\eta}\frac{\delta\omega}{\pi}\left[\underbrace{\int_0^{\delta\omega}\mathrm{d}\omega\sqrt{1-\frac{\omega^2}{\delta\omega^2}}}_{=\frac{\pi}{4}\delta\omega}-\frac{4}{\pi}\eta\delta\omega+\int_0^{\frac{4}{\pi}\eta\delta\omega}\mathrm{d}\omega f(\alpha,\omega)\right].\tag{45}$$

The last integral can be found as

$$\begin{aligned}\int_0^{\frac{4}{\pi}\eta\delta\omega}\mathrm{d}\omega f(\alpha,\omega) &= \frac{4}{\pi}\eta\delta\omega\left[\int_{-\frac{\pi}{4}}^{+\frac{\pi}{4}}\mathrm{d}\phi\cos(2\phi)-\int_{-\frac{\pi}{4}}^{\alpha-\frac{\pi}{4}}\mathrm{d}\phi\cos^2(2\phi)\sin^2(\phi-\alpha)-\int_{\alpha-\frac{\pi}{4}}^{+\frac{\pi}{4}}\mathrm{d}\phi\cos^2(2\phi)\cos^2(\phi-\alpha)\right]\\ &= \frac{4}{\pi}\left[\frac{3}{4}-\frac{\pi}{8}-\frac{\cos(4\alpha)}{12}\right].\end{aligned}\tag{46}$$

Finally, one finds Eq. (22). The magnetization $M(\alpha,t)$ can be found by a Fourier transform of the frequency distribution. One eventually arrives at

$$\begin{aligned}M(\alpha,t)=&-\frac{\eta}{1-\eta}{}_1F_2\left(-\frac{1}{2};\frac{1}{2},1;-\frac{\delta\omega^2t^2}{4}\right)\\ &+\int_{-\frac{\pi}{4}}^{\alpha-\frac{\pi}{4}}\mathrm{d}\phi\left[\frac{\cos\left(\frac{4}{\pi}\eta\delta\omega t\cos(2\phi)\sin^2(\phi-\alpha)\right)}{2[1-\eta]\sin^2(\phi-\alpha)}+\frac{2}{\pi}\frac{\eta\delta\omega t}{1-\eta}\cos(2\phi)\mathrm{Si}\left(\frac{4}{\pi}\eta\delta\omega t\cos(2\phi)\sin^2(\phi-\alpha)\right)\right]\\ &+\int_{\alpha-\frac{\pi}{4}}^{+\frac{\pi}{4}}\mathrm{d}\phi\left[\frac{\cos\left(\frac{4}{\pi}\eta\delta\omega t\cos(2\phi)\cos^2(\phi-\alpha)\right)}{2[1-\eta]\cos^2(\phi-\alpha)}+\frac{2}{\pi}\frac{\eta\delta\omega t}{1-\eta}\cos(2\phi)\mathrm{Si}\left(\frac{4}{\pi}\eta\delta\omega t\cos(2\phi)\cos^2(\phi-\alpha)\right)\right],\end{aligned}\tag{47}$$

where we used the identity of the incomplete Gamma function for purely imaginary arguments $\mathrm{Im}(\Gamma(0,\mathrm{i}x))=\mathrm{Si}(x)+\mathrm{sign}(x)\frac{\pi}{2}$ given in [40] with the sine integral Si. In the case of $\alpha=0$, the magnetization can be rewritten as

$$M(0,t)=-\frac{\eta}{1-\eta}{}_1F_2\left(-\frac{1}{2};\frac{1}{2},1;-\frac{\delta\omega^2t^2}{4}\right)+\int_0^1\frac{\mathrm{d}z}{\sqrt{1-z^2}}\left[\frac{\cos\left(\frac{2}{\pi}\eta\delta\omega tz[1+z]\right)}{[1-\eta][1+z]}+\frac{2}{\pi}\frac{\eta\delta\omega t}{1-\eta}z\mathrm{Si}\left(\frac{2}{\pi}\eta\delta\omega tz[1+z]\right)\right].\tag{48}$$

Appendix B. Non-centered vessels

So far, vessels are placed in the center of the voxel. However, the frequency distribution changes for non-centered vessels. In principle, the methods presented in Appendix A allow calculating the frequency distribution for arbitrary vessel position and arbitrary angle α. However, the expressions and their numerical implementation become complicated and, thus, we fix the angle $\alpha = 0^\circ$ and focus on vessel displacements ϵ in y-direction, see Fig. 10.

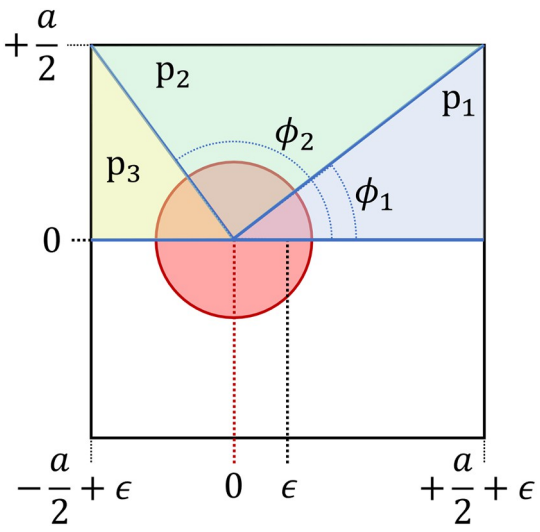

Fig. 10. Schematic illustration of a non-centered vessel. The case of $\alpha = 0^\circ$ and displacement ϵ along the y-direction is considered. Therefore, the contribution to the frequency distribution is divided into three different parts p_1, p_2 and p_3.

In close analogy to Appendix A, the frequency distribution is a sum over distinct contributions as shown in Fig. 10. The contribution of the inner cylinder p_{V_0} is given in Eq. (33). The frequency distribution is finally obtained as

$$p_\epsilon(\omega) = p_1(\omega) + p_2(\omega) + p_3(\omega) - p_{V_0}(\omega)\,. \tag{49}$$

Each contribution can be calculated in analogy to Appendix A. Thus, finally the frequency distribution can be obtained as

$$p_\epsilon(\omega) = \frac{\eta}{1-\eta}\frac{\delta\omega}{\pi\omega^2}\left[\sqrt{1-\frac{\omega^2}{\delta\omega^2}} - 1 + f_\epsilon(\omega)\right], \tag{50}$$

where $f_\epsilon(\omega)$ is given as

$$\begin{aligned}
f_\epsilon(\omega) \;=\; & \Theta(+\omega)\int_{\phi_1}^{\frac{\pi}{4}} \mathrm{d}\phi\cos(2\phi)\Theta\left(\frac{\pi}{4\eta}\frac{\omega}{\delta\omega} - \cos(2\phi)\sin^2(\phi)\right)\\
& + \Theta(+\omega)\int_{0}^{\phi_1} \mathrm{d}\phi\cos(2\phi)\Theta\left(\left[\frac{\pi}{4\eta} + \sqrt{\frac{\pi}{\eta}}\frac{\epsilon}{R} + \frac{\epsilon^2}{R^2}\right]\frac{\omega}{\delta\omega} - \cos(2\phi)\cos^2(\phi)\right)\\
& + \Theta(+\omega)\int_{\frac{3\pi}{4}}^{\pi} \mathrm{d}\phi\cos(2\phi)\Theta\left(\left[\frac{\pi}{4\eta} - \sqrt{\frac{\pi}{\eta}}\frac{\epsilon}{R} + \frac{\epsilon^2}{R^2}\right]\frac{\omega}{\delta\omega} - \cos(2\phi)\cos^2(\phi)\right)\\
& - \Theta(-\omega)\int_{\frac{\pi}{4}}^{\phi_2} \mathrm{d}\phi\cos(2\phi)\Theta\left(-\frac{\pi}{4\eta}\frac{\omega}{\delta\omega} + \cos(2\phi)\sin^2(\phi)\right)\\
& - \Theta(-\omega)\int_{\phi_2}^{\frac{3\pi}{4}} \mathrm{d}\phi\cos(2\phi)\Theta\left(-\left[\frac{\pi}{4\eta} - \sqrt{\frac{\pi}{\eta}}\frac{\epsilon}{R} + \frac{\epsilon^2}{R^2}\right]\frac{\omega}{\delta\omega} + \cos(2\phi)\cos^2(\phi)\right).
\end{aligned} \tag{51}$$

The first three integrals describe the function for positive frequencies ω, the last two integrals for negative frequencies. The angles ϕ_1 and ϕ_2 are measured between y-axis and diagonals of the cubic voxel as shown in Fig. 10:

$$\phi_1 = \arctan\left(\frac{1}{1+\frac{2\epsilon}{a}}\right) \tag{52}$$

$$\phi_2 = \pi - \arctan\left(\frac{1}{1-\frac{2\epsilon}{a}}\right). \tag{53}$$

The frequency distribution $p_\epsilon(\omega)$ is visualized in Fig. 11 for different displacements ϵ.

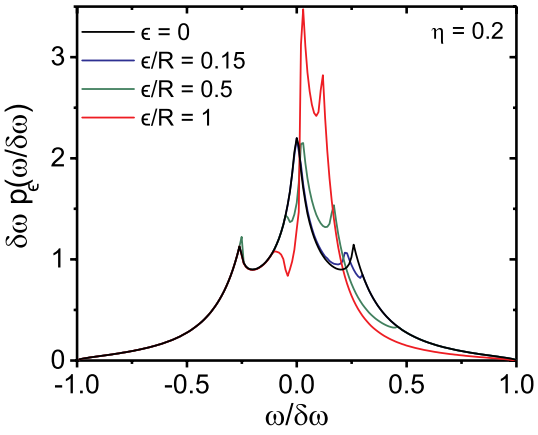

Fig. 11. Frequency distribution $p_\epsilon(\omega)$ for different displacements ϵ. For small displacements compared to the vessel radius, the frequency distribution shows only little changes, for large displacements, however, the peak structure of the frequency distribution is significantly disturbed.

For small displacements ϵ compared to the vessel radius R, the frequency distribution is only slightly changed, for large displacements, a prominent asymmetry of the frequency distribution is observed and the peak structure of the frequency distribution changes significantly. This goes along with a change of the relaxation time T_2'.

References

[1] Yablonskiy DA, Haacke EM. Theory of NMR signal behavior in magnetically inhomogeneous tissues: the static dephasing regime. Magn Reson Med 1994;32:749–63.

[2] Ogawa S, Lee TM, Kay AR, Tank DW. Brain magnetic resonance imaging with contrast dependent on blood oxygenation. Proc Natl Acad Sci USA 1990;87:9868–72.

[3] Sedlacik J, Rauscher A, Reichenbach JR. Obtaining blood oxygenation levels from MR signal behavior in the presence of single venous vessels. Magn Reson Med 2007;58(5):1035–44.

[4] Marques JP, Bowtell RW. Using forward calculations of the magnetic field perturbation due to a realistic vascular model to explore the BOLD effect. NMR Biomed 2008;21(6):553–65.

[5] Domsch S, Mie MB, Wenz F, Schad LR. Non-invasive multiparametric qBOLD approach for robust mapping of the oxygen extraction fraction. Z Med Phys 2014;24(3):231–42.

[6] Mulkern R, Haker S, Mamata H, Lee E, Mitsouras D, Oshio K, et al. Lung parenchymal signal intensity in MRI: a technical review with educational aspirations regarding reversible versus irreversible transverse relaxation effects in common pulse sequences. Concepts Magn Reson Part A 2014;43A:29–53.

[7] Buschle LR, Kurz FT, Kampf T, Wagner WL, Duerr J, Stiller W, et al. Dephasing and diffusion on the alveolar surface. Phys Rev E 2017;95(2-1):022415.

[8] Gyngell ML. The steady-state signals in short-repetition-time sequences. J Magn Reson 1989;81(3):474–83.

[9] Scheffler K, Hennig J. Is TrueFISP a gradient-echo or a spin-echo sequence? Magn Reson Med 2003;49(2):395–7.

[10] Ganter C. Static susceptibility effects in balanced SSFP sequences. Magn Reson Med 2006;56(3):687–91.

[11] Baez-Yanez MG, Ehses P, Mirkes C, Tsai PS, Kleinfeld D, Scheffler K. The impact of vessel size, orientation and intravascular contribution on the neurovascular fingerprint of BOLD bSSFP fMRI. Neuroimage 2017;163:13–23.

[12] Sedlacik J, Boelmans K, Löbel U, Holst B, Siemonsen S, Fiehler J. Reversible, irreversible and effective transverse relaxation rates in normal aging brain at 3 T. Neuroimage 2013;84:1032–41.

[13] Ziener CH, Kampf T, Melkus G, Herold V, Weber T, Reents G, et al. Local frequency density of states around field inhomogeneities in magnetic resonance imaging: effects of diffusion. Phys Rev E 2007;031915:76.

[14] Buschle LR, Kurz FT, Kampf T, Triphan SMF, Schlemmer HP, Ziener CH. Diffusion-mediated dephasing in the dipole field around a single spherical magnetic object. Magn Reson Imaging 2015;33:1126–45.

[15] Bauer WR, Nadler W, Bock M, Schad LR, Wacker C, Hartlep A, et al. Theory of coherent and incoherent nuclear spin dephasing in the heart. Phys Rev Lett 1999;83:4215–8.

[16] Ziener CH, Kampf T, Reents G, Schlemmer HP, Bauer WR. Spin dephasing in a magnetic dipole field. Phys Rev E 2012;051908:85.

[17] Ziener CH, Kurz FT, Kampf T. Free induction decay caused by a dipole field. Phys Rev E 2015;032707:91.

[18] Kurz FT, Ziener CH, Rückl M, Hahn A, Sturm VJF, Zhang K, et al. The influence of spatial patterns of capillary networks on transverse relaxation. Magn Reson Imaging 2017;40:31–47.

[19] Sedlacik J, Rauscher A, Reichenbach JR. Quantification of modulated blood oxygenation levels in single cerebral veins by investigating their MR signal decay. Z Med Phys 2009;19(1):48–57.

[20] Nadler W, Schulten K. Mean relaxation time approximation for dynamical correlation functions in stochastic systems near instabilities. Z Phys B 1985;59:53–61.

[21] Ziener CH, Bauer WR, Jakob PM. Frequency distribution and signal formation around a vessel. Magn Reson Mater Phys 2005;18:225–30.

[22] Krogh A. The supply of oxygen to the tissues and the regulation of the capillary circulation. J Physiol 1919;52:457–74.

[23] Cheng YC, Haacke EM. Predicting BOLD signal changes as a function of blood volume fraction and resolution. NMR Biomed 2001;14(7–8):468–77.

[24] Ziener CH, Kampf T, Melkus G, Jakob PM, Schlemmer HP, Bauer WR. Signal evolution in the local magnetic field of a capillary - analogy to the damped driven harmonic oscillator. Magn Reson Imaging 2012;30:540–53.

[25] Kurz FT, Kampf T, Buschle LR, Heiland S, Schlemmer HP, Bendszus M, et al. CPMG relaxation rate dispersion in dipole fields around capillaries. Magn Reson Imaging 2016;34:875–88.

[26] Cheng YC, Haacke EM, Yu YJ. An exact form for the magnetic field density of states for a dipole. Magn Reson Imaging 2001;19:1017–23.

[27] Herráez MA, Burton DR, Lalor MJ, Gdeisat MA. Fast two-dimensional phase-unwrapping algorithm based on sorting by reliability following a noncontinuous path. Appl Opt 2002;41(35):7437–44.

[28] Scheenen TWJ, Klomp DWJ, Wijnen JP, Heerschap A. Short echo time 1H-MRSI of the human brain at 3 T with minimal chemical shift displacement errors using adiabatic refocusing pulses. Magn Reson Med 2008;59(1):1–6.

[29] Bottomley PA. Spatial localization in NMR spectroscopy in vivo. Ann N Y Acad Sci 1987;508:333–48.

[30] Dagher J, Du YP. Efficient and robust estimation of blood oxygenation levels in single cerebral veins. Med Biol Eng Comput 2012;50(5):473–82.

[31] Schenck JF. The role of magnetic susceptibility in magnetic resonance imaging: MRI magnetic compatibility of the first and second kinds. Med Phys 1996;23(6):815–50.

[32] Haacke EM, Thompson MR, Brown RW, Venkatesan R. Magnetic resonance imaging: physical principles and sequence design. New York: Wiley; 1999.

[33] Dickson JD, Ash TW, Williams GB, Sukstanskii AL, Ansorge RE, Yablonskiy DA. Quantitative phenomenological model of the BOLD contrast mechanism. J Magn Reson 2011;212:17–25.

[34] Spees WM, Yablonskiy DA, Oswood MC, Ackerman JJH. Water proton MR properties of human blood at 1.5 Tesla: magnetic susceptibility, T1, T2, T2*, and non-Lorentzian signal behavior. Magn Reson Med 2001;45:533–42.

[35] Bauer WR, Nadler W, Bock M, Schad LR, Wacker C, Hartlep A. Theory of the BOLD effect in the capillary region: an analytical approach for the determination of T2 in the capillary network of myocardium. Magn Reson Med 1999;41:51–62.

[36] Seppenwoolde JH, van Zijtveld M, Bakker CJ. Spectral characterization of local magnetic field inhomogeneities. Phys Med Biol 2005;50:361–72.

[37] Reichenbach JR, Haacke EM. High-resolution BOLD venographic imaging: a window into brain function. NMR Biomed 2001;14(7–8):453–67.

[38] Fan AP, Bilgic B, Gagnon L, Witzel T, Bhat H, Rosen BR, et al. Quantitative oxygenation venography from MRI phase. Magn Reson Med 2014;72(1):149–59.

[39] Buschle LR, Ziener CH, Zhang K, Sturm VJF, Kampf T, Hahn A, et al. Vessel radius mapping in an extended model of transverse relaxation. Magn Reson Mater Phys 2018;31:531–51.

[40] Oldham KB, Myland J, Spanier J. An atlas of functions: with equator, the atlas function calculator. Springer Science & Business Media; 2010.